



Contents lists available at ScienceDirect

Medical Image Analysis

journal homepage: www.elsevier.com/locate/media

Instance-level quantitative saliency in multiple sclerosis lesion segmentation

Federico Spagnolo^{a,b,c,d}, Nataliia Molchanova^{d,e,f}, Roger Schaer^d, Meritxell Bach Cuadra^{e,f}, Mario Ocampo Pineda^{a,b,c}, Lester Melie-Garcia^{a,b,c}, Cristina Granziera^{a,b,c}, Vincent Andrearczyk^{d,#}, Adrien Depeursinge^{d,g,#,*}

^aTranslational Imaging in Neurology (ThInk) Basel, Department of Medicine and Biomedical Engineering, University Hospital Basel and University of Basel, Basel, Switzerland

^bDepartment of Neurology, University Hospital Basel, Basel, Switzerland

^cResearch Center for Clinical Neuroimmunology and Neuroscience Basel (RC2NB), University Hospital Basel and University of Basel, Basel, Switzerland

^dMedGIFT, Institute of Informatics, School of Management, HES-SO Valais-Wallis University of Applied Sciences and Arts Western Switzerland, Sierre, Switzerland

^eCIBM Center for Biomedical Imaging, Lausanne, Switzerland

^fRadiology Department, Lausanne University Hospital (CHUV) and University of Lausanne, Lausanne, Switzerland

^gNuclear Medicine and Molecular Imaging Department, Lausanne University Hospital (CHUV), Lausanne, Switzerland

ARTICLE INFO

Article history:

Keywords: MRI, Multiple Sclerosis, XAI, Deep learning

ABSTRACT

In recent years, explainable methods for artificial intelligence (XAI) have tried to reveal and describe models' decision mechanisms in the case of classification tasks. However, XAI for semantic segmentation and in particular for single instances has been little studied to date. Understanding the process underlying automatic segmentation of single instances is crucial to reveal what information was used to detect and segment a given object of interest (e.g., a lesion in medical imaging or a car in a natural image) among others of the same class. This information can serve as a basis to (i) identify application contexts (e.g., lesion location) where the networks may deliver sub-optimal performance, (ii) optimize their internal architecture (e.g., patch size), and (iii) justify the model's decisions to the end users.

In this study, we proposed two instance-level explanation maps for semantic segmentation based on SmoothGrad and Grad-CAM++ methods. Then, we investigated their relevance for the detection and segmentation of white matter lesions (WML), a magnetic resonance imaging (MRI) biomarker in multiple sclerosis (MS). 687 patients diagnosed with MS for a total of 4043 FLAIR and MPRAGE MRI scans (baseline, follow-ups and WM lesion masks annotated by three expert clinicians) were collected at the University Hospital of Basel, Switzerland. Data were randomly split into training, validation and test sets (containing respectively 585, 94 and 35 patients) to train a 3D U-Net for MS lesion segmentation. With a Dice score of 0.60 and a normalized Dice score of 0.71, we observed 3050 true positive (TP), 1818 false positive (FP), and 789 false negative (FN) cases. We generated instance-level explanation maps for semantic segmentation, by developing two XAI methods based on SmoothGrad and Grad-CAM++. The extent of information used by the U-Net during inference was investigated with the two new instance-based XAI methods at different levels: 1) the distribution of gradients in saliency maps with respect to both input MRI sequences; 2) a comparison between TP, FP, FN and true negative (TN) volumes; 3) the model's response and saliency map in the case of synthetic lesions in various image locations (in the background, in the WM, and in the background with part of the perilesional tissue); 4) the amount of perilesional tissue needed by the model to segment a lesion.

Saliency maps (based on SmoothGrad) in FLAIR showed positive values inside a lesion and negative in its neighborhood. FLAIR input images consistently had a higher impact on predictions than MPRAGE in TP, FN, FP and TN volumes. Peak values

of saliency maps generated for these four groups of volumes presented distributions that differ significantly from one another, suggesting that the quantitative nature of the proposed saliency could be used to identify errors. Artificially isolated lesions (i.e., surrounded by a black background) were not detected as lesions. Contextual information of $\sim 7mm$ around the lesion border was required for their segmentation.

In conclusion, the two proposed quantitative methods provide quantitative instance-level explanations in semantic segmentation tasks, revealing fundamental insights into the decision process of a deep learning MS lesion segmentation network.

© 2024 Elsevier B. V. All rights reserved.

1. Introduction

Multiple sclerosis (MS) is an autoimmune neurological disease, which affects people at a relatively young age, presenting a considerable impact on the quality of life (Kołtuniuk et al., 2023). One of the most important biomarkers in MS are white matter (WM) lesions reported on magnetic resonance imaging (MRI) (Yang et al., 2022). The standard MRI sequences used for MS diagnosis and follow-up (Thompson et al., 2017) are the fluid attenuated inversion recovery (FLAIR) and T1-weighted (T1-w) contrast, such as the magnetisation-prepared rapid gradient echo (MPRAGE) (Hemond C and Bakshi, 2018). WM lesions appear as hyperintense in FLAIR and as hypointense in T1-w images.

These lesions are usually manually or semi-automatically annotated by clinicians with several years of experience, through a time-consuming process, subject to inter-observer variations. Despite many efforts to automate the process of lesion detection and segmentation with deep learning (DL) methods (Alrabai et al., 2022; Zeng et al., 2020; Ma et al., 2022; Diaz-Hurtado et al., 2022; Commowick et al., 2023), their clinical integration is being jeopardized by two main issues:

1. The “black box” nature of the models (Baselli et al., 2020). Since these methods contain many layers and millions of parameters it is hard to interpret and explain which are the drivers for a particular decision, i.e., which rules were used to identify and segment a given lesion of interest.
2. Insufficient clinical validation of the models, described in Spagnolo et al. (2023).

To address the first issue, research in explainable AI (XAI) may play a decisive role. XAI has the potential to support trustworthy AI via better understanding (e.g., decision rules, biases) and optimization of DL models (Kobayashi and Alam, 2024). However, XAI for semantic segmentation and in particular for detecting and contouring single instances of interest has been little studied to date. Semantic segmentation is a computer vision task, where labels are associated with every pixel of an image. In the case of WM lesions, such as depicted in Fig.1a with four distinct lesion instances, the segmented plaques appear as disconnected volumes in the MRI. In general, objects may appear as connected, and can be segmented into separate entities through instance segmentation. Instance segmentation can extract supplementary information from the image, such as the number of objects of the same class (as person one to five in Fig.1b). Treating separate instances would be crucial to understand the mechanisms underlying automatic detection and segmentation of a given object of interest (e.g., a lesion in medical imaging or a person in a natural image) among other objects of the same class. This also applies to the case of MS lesions, where plaques can be subdivided based on their location in the brain, or the stage of the disease (Jonkman et al., 2015). Specifically, considering separate instances would be important to generate instance-specific explanations not only for diagnosis at single time-points, but also for disease monitoring in follow-ups.

Introducing instance-level explanation methods could facilitate a better understanding of AI’s segmentation of single instances. In addition to the case of MS, such methods could be applicable to any pathology involving sparse lesions, beyond MRI, and possibly to any segmentation task.

1.1. Related work

1.1.1. Classification task

An exhaustive review of XAI models and applications can be found in Saranya and Subhashini (2023). For convolutional neural networks (CNN) in a classification scenario, a widely used ad-hoc method is pixel attribution (or saliency maps), in which pixels are colored based on their contribution to the classification. To this end, vanilla gradients (Simonyan et al., 2013) is a method based on forward and backward propagation through the network. First, an input image (for instance a 3D image) is fed forward through the network and a class score is computed. Then, the gradient of the score with respect to the input — or a layer — is

*Corresponding author: Tel.: +41-27-207-9038;

e-mail: adrien.depeursinge@hevs.ch (Adrien Depeursinge)

#These authors contributed equally to this work.

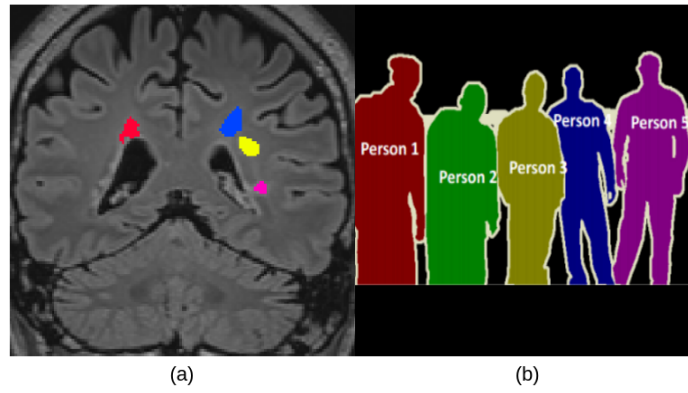


Fig. 1. (a) FLAIR MRI presenting WM lesions segmented as separate entities, and (b) example of instance segmentation retrieved from Varatharasan *et al.* (2019).

calculated backwards to form a map, which represents positive and negative contributions of input voxels to the classification of the image. Maps generated with this method are easy to compute and visualize, but also noisy and sensitive to small changes in the input (de Vries *et al.*, 2023). To partially address these problems, Smilkov *et al.* (2017) introduced a method called SmoothGrad (SG). A more stable output is obtained by feeding multiple noisy versions of the input image to the network and averaging the obtained saliency maps. Some recent applications can be found in Goh *et al.* (2021) and Agarwal *et al.* (2021).

Another widely used XAI method for classification, is Grad-CAM (Selvaraju *et al.*, 2017). The gradients of a class score — with respect to activation maps of a given layer — are spatially aggregated through global average pooling. This way, a weight is computed for each activation map, representing its relevance. These weights are then employed to calculate the visualization heatmap as a linear combination of the activation maps, followed by a ReLU to focus on features positively influencing the class score. However, this method presented a low accuracy when the image contained multiple instances of the same class. To overcome this, Chattopadhyay *et al.* (2018) described Grad-CAM++, where the weights are obtained through a weighted average of the gradients.

SG and Grad-CAM++ can be seen as complementary methods. The first provides local-level information and works well in identifying the impact of multiple input channels (or modalities), since the gradients flow all the way back to the inputs. The second can generate more stable heatmaps, and probe specific layers of the network. However, both algorithms were originally designed for classification tasks, such as in Rajpurkar *et al.* (2017). This means that, in general, the output y of a multi-class classification network is a vector of C scalar values, where C is the number of classes. In the case of semantic segmentation, y is a set of C tensors (2D or 3D images) containing segmentation scores for each class (Fig. 2).

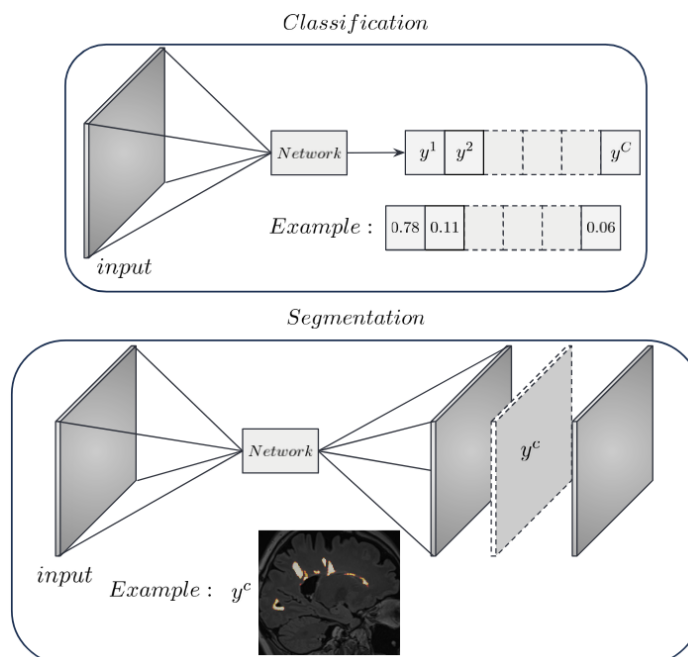


Fig. 2. Input-output dimensions for a classification (top) and a semantic segmentation (bottom) task.

Indeed, computing a gradient map for all the output voxels would not be convenient or meaningful in a segmentation scenario. The number of maps per patient would be excessive, thus impractical for the end-user, especially for a clinician. Additionally, the computation time would be unnecessarily high.

1.1.2. Segmentation task

A straightforward way to adapt explainable methods to semantic segmentation would be, for a given class c , to aggregate all the spatial predictions y^c into a single scalar (e.g., a summation) and compute its gradients. However, this approach yields to confusing and hardly interpretable maps, where the relevance of input voxels to the segmentation scores of all output voxels (even those not segmented as part of class c) are merged together, as reported in Fig. 3. Indeed, these results do not provide any kind of explanation to the segmentation of a particular instance of the considered class c .

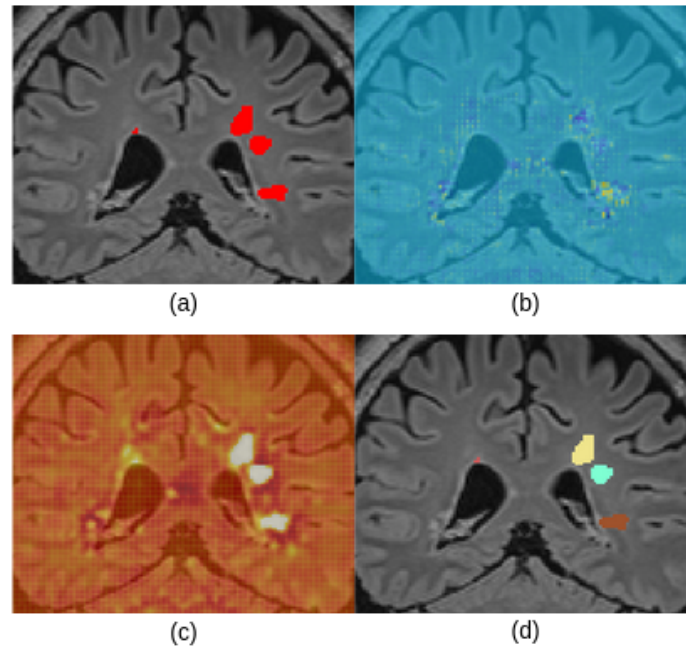


Fig. 3. (a) The output of a semantic segmentation network showing several instances of the considered class. SmoothGrad (b) and Grad-CAM (c) applied to all the spatial predictions. (d) How can we explain the segmentation of a particular lesion of interest (e.g., the yellow instance) ?

Recent works, such as Mahapatra et al. (2022) and Arun et al. (2021), state clearly that saliency maps were not initially developed for segmentation tasks and, therefore, no explicit methods are currently available to do so. In Arun et al. (2021), this statement was used to warn the readers about potential problems related to the misuse of XAI in clinical practice, and proposed pixel-level metrics to evaluate saliency maps. Singh et al. (2022) applied saliency maps to classification networks, while adopting uncertainty maps instead to explain skin lesion segmentation.

First steps towards the use of XAI in segmentation were taken in the work of Wickstrøm et al. (2020). They used guided backpropagation (Simonyan et al., 2013) to generate saliency maps for the explanation of colorectal polyp segmentation. Their saliency maps were obtained by aggregating all the positive spatial predictions. Similarly, Vinogradova et al. (2020) generated heatmaps by using the first version of Grad-CAM (Selvaraju et al., 2017), and aggregating only output voxels segmented as part of a target class c . The authors employed a U-Net and the dataset Cityscapes (Cordts et al., 2016) to perform semantic segmentation.

While these approaches lead to a possible class-level explanation for semantic segmentation, they still do not provide any instance-level information, such as which input voxels were exploited to segment a specific instance. In addition, these methods do not provide quantitative saliency maps, which means these maps do not allow to interpret their absolute values across images or objects of interest to, e.g., distinguish false positives or false negatives from true positives.

To address the aforementioned limitations, this paper presents the adaptation of SG and Grad-CAM++ to obtain quantitative and instance-level explanation maps, and their application to WM lesion segmentation in MS.

2. Material and methods

2.1. Dataset and model

687 patients diagnosed with MS for a total of 4023 FLAIR and MPRAGE MRI scans (age=45.2±12.2, 433 females, SIEMENS Avanto/Espree/Symphony 1.5T and Prisma/Skyra/Verio/MAGNETOM Vida 3T, 1mm isotropic, Expanded Disability Status Scale

median of 2.5 [0-9]) were collected at the University Hospital of Basel, Switzerland. Three expert clinicians annotated WM lesion masks from baseline and follow-ups. Data were randomly split into training, validation and test sets (containing 560, 90 and 37 patients with 3369, 553 and 101 scans, respectively; training/validation set's and test set's mean lesions number of 52.9 ± 36.4 and 42.3 ± 21.4 per patient) to train and evaluate a 3D U-Net (Çiçek *et al.*, 2016) for WM lesion segmentation, using patches of dimensions 96^3 . The split was performed at patient level to ensure that images from the same patient belong to the same split. We adopted a linear combination of normalized Dice (Raina *et al.*, 2023) and blob (Kofler *et al.*, 2022) losses to tackle instance imbalance within a class and bias towards the occurrence of positive class (Maier-Hein *et al.*, 2022). Pre-processing steps included the registration of FLAIR images to MPRAGE space using the *elastix* toolbox (Klein *et al.*, 2009; Shamonin *et al.*, 2014), N4 bias field inhomogeneity correction (Tustison *et al.*, 2010) and z -score intensity normalisation. The described model achieved a Dice score of 0.60 and a normalized Dice score of 0.71 on the test set, detecting 4868 WM lesion candidates out of the 3839 manually annotated.

2.2. Notations

Following Depeursinge *et al.* (2020), we noted a discrete image as a D -dimensional function of the variable $\mathbf{v} = (v_1, \dots, v_D) \in \mathbb{Z}^D$, taking values $x[\mathbf{v}] \in \mathbb{R}$. A subset Γ of \mathbb{Z}^D was considered in practice for the spatial image domain with dimensions $N_1 \times \dots \times N_D$ as possible values for the index vector $\mathbf{v} \in \Gamma$. We also referred to the lesion domain Ω as a subset of the image domain with cardinality (i.e., number of voxels) $|\Omega|$, such that $\Omega \subset \Gamma \subset \mathbb{Z}^D$.

Input images $x[\mathbf{v}]$ performing a forward pass through the network resulted in logits $y(x)[\mathbf{v}] \in \mathbb{R}$, where $\mathbf{v} \in \Gamma$ is a map of raw output values, which had the exact same dimensions as the input $x[\mathbf{v}]$ since we considered a segmentation task. We use the simplified notation $y[\mathbf{v}]$ when the input x is unambiguous. This raw output was generally interpreted as a probability map (e.g., after Softmax), which was binarized using a threshold $t = 0.3$ yielding the best normalized Dice score during validation. Then, each connected component (with a minimum volume size of $5mm^3$) of the binary map was considered as a specific WM lesion instance, forming the subdomain Ω .

2.3. Gradient-based saliency maps

During the backward pass and for each element of $y(x)[\mathbf{v}]$, the gradients with respect to all the elements of input $x[\mathbf{v}]$ can be computed. These gradients can be visualized as an image with same dimensions as the input and output, constituting a first method to construct saliency maps. This approach is usually referred to as vanilla gradients (Simonyan *et al.*, 2013).

The SG algorithm Smilkov *et al.* (2017) tackled the problem of instability of vanilla gradients maps: the gradient of logits $y(x_n)$ is computed N times based on artificially noised versions of the input $x_n[\mathbf{v}]$. The authors demonstrated that the average M of these maps is more stable than vanilla gradients maps:

$$M[\mathbf{v}] = \frac{1}{N} \sum_{n=1}^N \frac{\partial y(x_n)}{\partial x_n[\mathbf{v}]} \quad (1)$$

2.3.1. Instance-level saliency (gradients)

This approach was introduced in a classification paradigm. However, with segmentation models, there are predictions for each output voxel \mathbf{v} . As a result, the visualisation of many heatmaps for a single output voxel is neither convenient nor meaningful. Hence, we adapted the original method to the segmentation task by aggregating these heatmaps. For a given lesion, the implementation consists of:

1. Injecting a Gaussian noise $\mathcal{N}(0, \sigma)$ with standard deviation σ to obtain N noisy versions of the input,
2. Computing a collection of saliency maps for all output voxels in the domain Ω of the lesion,
3. Determining the average map from this collection of maps,
4. Repeating steps 1-3 and combining these $N = 50$ saliency maps ($\sigma = 0.05$) to obtain a single one.

Steps 2 and 3 are illustrated in Fig. 4. Eq.(2) details the computation of lesion-level saliency maps $M_{\Omega}^{\text{gradient}}[\mathbf{v}] \in \mathbb{R}$ combining gradients calculated from each output voxel of a lesion. A separate saliency map is generated for each input modality (two in our case) allowing us to investigate their respective contribution.

$$M_{\Omega}^{\text{gradient}}[\mathbf{v}] = \frac{1}{N|\Omega|} \sum_{n=1}^N \sum_{\mathbf{v}' \in \Omega} \frac{\partial y(x_n)[\mathbf{v}']}{\partial x_n[\mathbf{v}]} \quad (2)$$

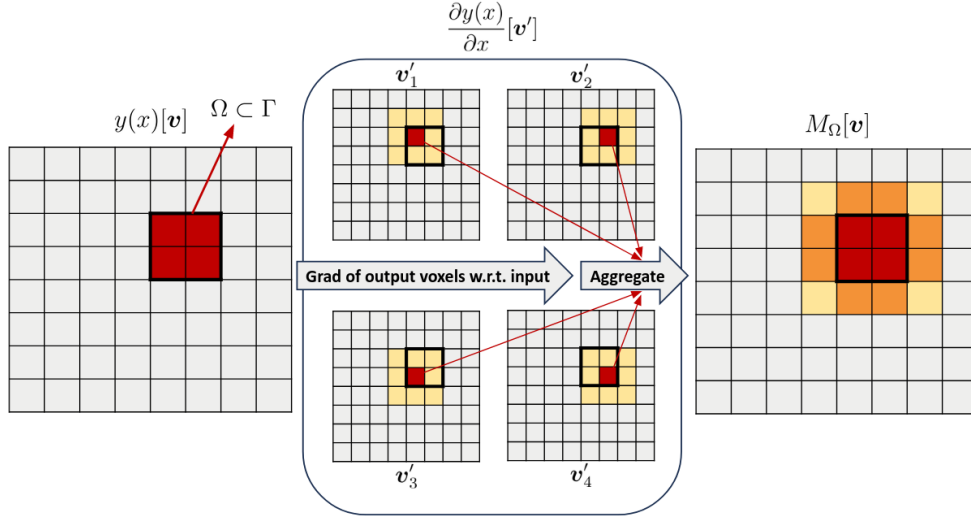


Fig. 4. Overview of the proposed adaptation of SG to segmentation.

2.3.2. Quantitative saliency maps: maximum versus average aggregation

The advantage of $M_{\Omega}^{\text{gradient}}[\mathbf{v}]$ is that it shows whether voxels outside the lesion domain Ω impact the prediction of voxels belonging to Ω . However, the lesion domain's dimensions may range from a few voxels to a considerable volume. The greater the lesion size, the more extended the potential distance between two voxels $p, q \in \Omega$. A long-distance means that the saliency map generated for the voxel p will present a low gradient value for q . The same principle applies to regions of the input far away from a lesion: their contribution to the prediction is low. As a consequence, the average over the lesion domain Ω in Eq.(2) will cause gradient values in $M_{\Omega}^{\text{gradient}}[\mathbf{v}]$ for extensive lesions to be systematically lower. Thus, following this method, the voxel values in saliency maps generated for different Ω (lesions) would not be comparable.

To this end, we propose Eq.(3), a slightly modified version of Eq.(2) where the average of saliency maps generated from each element of Ω is replaced by the voxel-wise maximum with sign:

$$M_{\Omega}^{\text{gradient}}[\mathbf{v}] = \frac{1}{N} \sum_{n=1}^N D_{\text{argmax}_{v'} |D_{v'}^n|}, \text{ where } D_{v'}^n = \frac{\partial y(x_n)[\mathbf{v}']}{\partial x_n[\mathbf{v}]} \quad (3)$$

2.4. Saliency maps based on Grad-CAM++

The second proposed method is based on Grad-CAM++ (Chattopadhyay et al., 2018) that we first recall here. We generated, for a given layer of a network, a heatmap M as a linear combination between weights $\{\omega^k\}_{k=1}^K$ and activation maps $\{A^k\}_{k=1}^K$. The activation maps of the selected layer may have different dimensions. In this case, the final heatmap is upsampled to the input dimensions. For the sake of simplicity, we defined the domain of the activation maps and that of the input image to be the same (i.e., activations from the last layer since we have a segmentation architecture): Γ , with values $A^k[\mathbf{v}] \in \mathbb{R}$. Following Vinogradova et al. (2020), to compute the gradients, we considered y' as the sum of logits $y[\mathbf{v}]$ higher than a threshold t , as in Eq.(5). Then, each weight ω^k is computed using the gradients of y' - with respect to the k^{th} activation map A^k - and a coefficient $\alpha^k[\mathbf{v}]$. We have

$$M^{\text{GradCAM}}[\mathbf{v}] = \text{Relu} \left(\sum_k \omega^k \cdot A^k[\mathbf{v}] \right), \quad (4)$$

$$y' = \sum_{\mathbf{v} | y[\mathbf{v}] > t} y[\mathbf{v}], \quad (5)$$

$$\omega^k = \sum_{\mathbf{v} \in \Gamma} \alpha^k[\mathbf{v}] \cdot \text{Relu} \left(\frac{\partial y'}{\partial A^k[\mathbf{v}]} \right), \quad (6)$$

$$\alpha^k[\mathbf{v}] = \frac{\frac{\partial^2 y'}{\partial (A^k[\mathbf{v}])^2}}{2 \cdot \frac{\partial^2 y'}{\partial (A^k[\mathbf{v}])^2} + \sum_{\mathbf{v}' \in \Gamma} (A^k[\mathbf{v}'] \cdot \frac{\partial^3 y'}{\partial (A^k[\mathbf{v}])^3})}, \quad (7)$$

where \mathbf{v} and \mathbf{v}' correspond to a different indexing over the domain Γ . A graphical representation of this method is reported in Fig. 5.

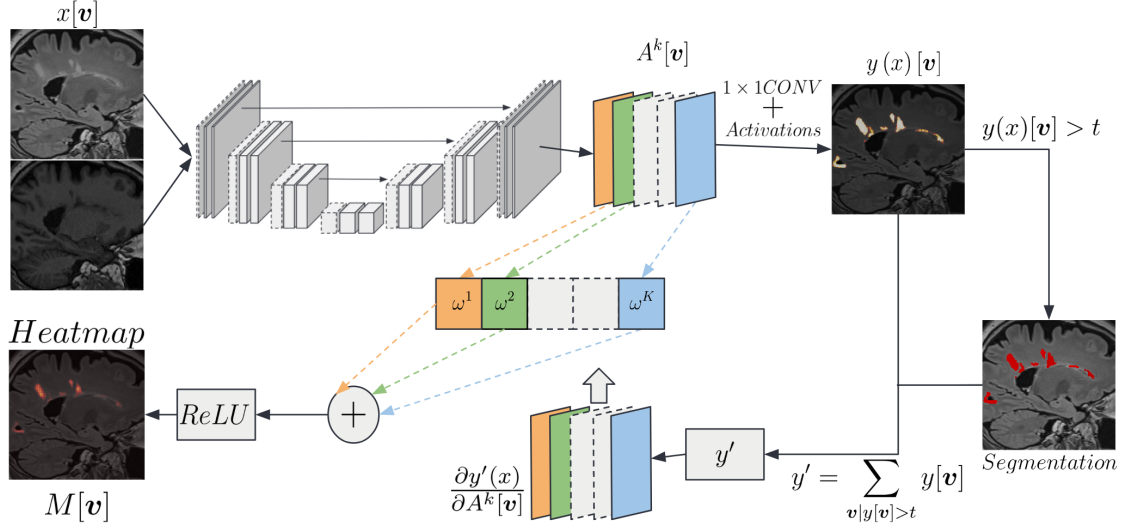


Fig. 5. Overview of Grad-CAM++, generating a class-level explanation heatmap, similarly to Vinogradova *et al.* (2020), adapted for segmentation.

2.4.1. Instance-level saliency (Grad-CAM++)

The simple adaptation of Grad-CAM++ to segmentation presented above generated a class-level explanation for semantic segmentation by merging contributions to different lesion instances. The impact of input regions on different parts of the output was combined by:

- Considering the gradients of a subset y' of logits $y[v]$,
- Assigning a single weight ω^k for each feature map A^k .

However, it would be useful to know which input voxels influenced the segmentation of a given instance (e.g., a lesion). To adapt the algorithm to an instance-level explanation, we considered two steps. First, the gradients of y were computed from the domain Ω of one lesion, as in Eq.(9). Then, the summation in Eq.(6) over Γ to compute weights was removed to retain a weight for each element of a feature map. This was needed to prevent the activation of other instances to emerge, and to select only the activation in Ω . Eq.(8) and Eq.(10) represent the proposed heatmap M_t^{GradCAM} provided by the modified Grad-CAM++ method, and the weights $\omega^k[v]$:

$$M_{\Omega}^{\text{GradCAM}}[v] = \text{Relu} \left(\sum_k \omega^k[v] \cdot A^k[v] \right), \quad (8)$$

$$y' = \sum_{v \in \Omega} y[v], \quad (9)$$

$$\omega^k[v] = \alpha^k[v] \cdot \text{Relu} \left(\frac{\partial y'}{\partial A^k[v]} \right), \quad (10)$$

where $\alpha^k[v]$ were obtained as in Eq. (7). An overview of the proposed adaptation of Grad-CAM++ to segmentation is illustrated in Fig. 6.

The code for the computation of explainable maps through both methods is publicly available at the following GitHub repository: <https://github.com/federicospagnolo/IES.git>.

2.5. Experiments

The described methodologies were applied to the entire test set, obtaining saliency maps for 3050 true positive (TP), 1818 false positive (FP), 789 false negative (FN), and 1010 true negative volumes (TN). TP and FP predictions were defined as having, respectively, a non-zero and zero overlap with ground truth (GT). FN predictions were considered as GT segmentations with zero overlap with the predicted lesion mask. To limit partial volume effects in these first three groups, a minimum volume size of 5mm^3 was set for each connected component, using a connectivity of 2. TN examples were generated by randomly sampling ten spherical volumes (93mm^3) inside each patient's brain and skull, excluding volumes intersecting GT and prediction masks. The size of the TN volumes was decided based on the average lesion volume in the GT masks of the test set.

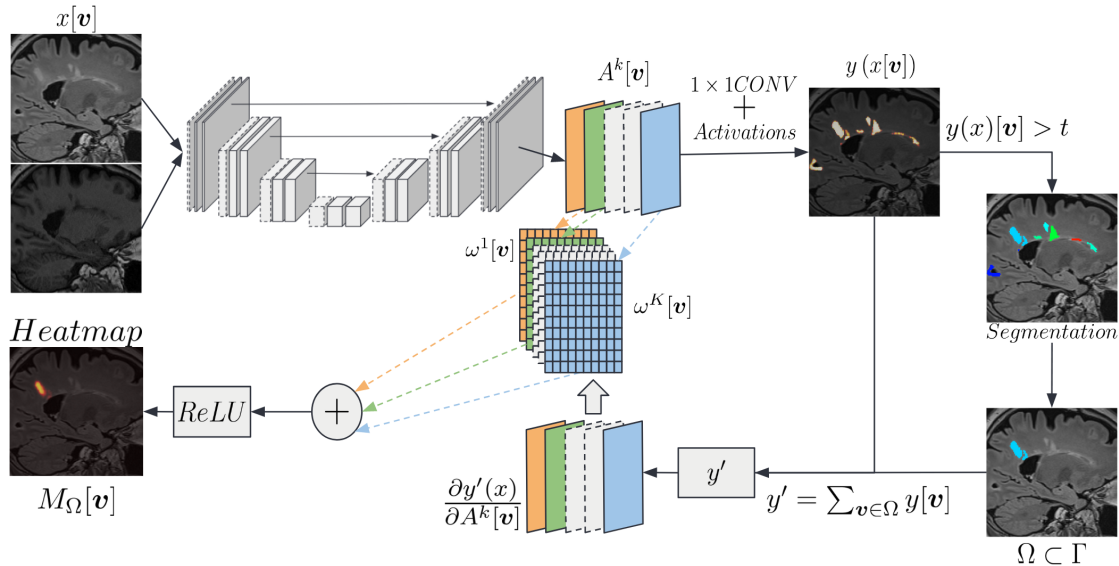


Fig. 6. Overview of the proposed adaptation of Grad-CAM++, generating an instance-level explanation heatmap.

The information exploited by the U-Net during inference for the segmentation of specific WM lesions was assessed with several experiments. Throughout these tests, the max aggregation method (see Material and methods 2.3.2) was selected to be used, thanks to its ability to provide quantitative information. This only applies to the saliency based on SG.

First (results in Section 3.2), the distribution of positive and negative values in saliency maps was observed to reveal potential patterns concerning recurring locations of positive/negative values with respect to Ω . An analysis of these distributions allowed a statistical comparison between gradient values computed with respect to FLAIR and MPRAGE. As a consequence, it was possible to isolate the contribution of both input sequences to the prediction of single lesions. In this analysis, we discarded gradient values between -0.1 and 0.1 in order to focus on voxels with a higher attention level.

Second (results in Section 3.3), we quantitatively compared the distribution of maximum and minimum saliency maps' values, for all predictions categories (i.e., TP, FP, FN and TN) to investigate if absolute saliency values can be used to flag potential detection errors. Furthermore, a two-sided Mann Whitney U test (McKnight and Najab, 2010) was run to statistically compare these groups.

To understand the model's level of specificity in segmenting MS lesions in the WM, we designed three additional qualitative experiments on a batch of 10 patients, in which we observed the model's behavior on synthetic lesions (results in Section 3.4). A first experiment was conducted, moving a clearly visible WM lesion to a different part of the WM, which originally presented no lesions. A similar approach was followed when inserting the same lesion outside the skull. A third experiment consisted of a compromise: the lesion, along with part of its surrounding healthy tissue (3mm from lesion border), was moved outside the skull. For all these cases, the model's prediction and saliency maps were examined.

In light of the results observed during the described tests, we designed a more specific experiment on the entire test set: the analysis of the needed amount of contextual information surrounding a lesion to obtain a segmentation (results in Section 3.5). We selected lesions with size close to the average of the entire dataset, i.e., from 90 to 120mm³, obtaining a total of 178 lesions. Initially, all voxel intensities were set to zero, but those of the lesion: this step was called iteration 0. Then, we gradually reassigned the original intensity to surrounding voxels through morphological 3D dilation, iterating this process 25 times. With the final iteration, the model was seeing a volume of surrounding tissue at a maximum of 25mm distance from the lesion's edges. At each iteration, the following metrics were recorded:

- The average and standard deviation across lesions of the mean prediction score (after Softmax) in Ω ,
- The number of segmented lesions.

In this experiment, each lesion was considered detected when at least one voxel in Ω reached a prediction score above the threshold $t = 0.3$.

3. Results

3.1. Maximum versus average aggregation for quantitative saliency maps

Considering only saliency based on SG, we compared the saliency maps obtained with either the average (Eq.(2)) or the maximum (Eq.(3)) aggregation method. As reported for an example lesion in Fig. 7, the saliency maps generated with the maximum

presented values that were comparable to those obtained for smaller lesions while preserving the proportion of positive and negative values according to the lesion properties. In the case of the method based on SG, the results in the following sections are obtained using the max aggregation method.

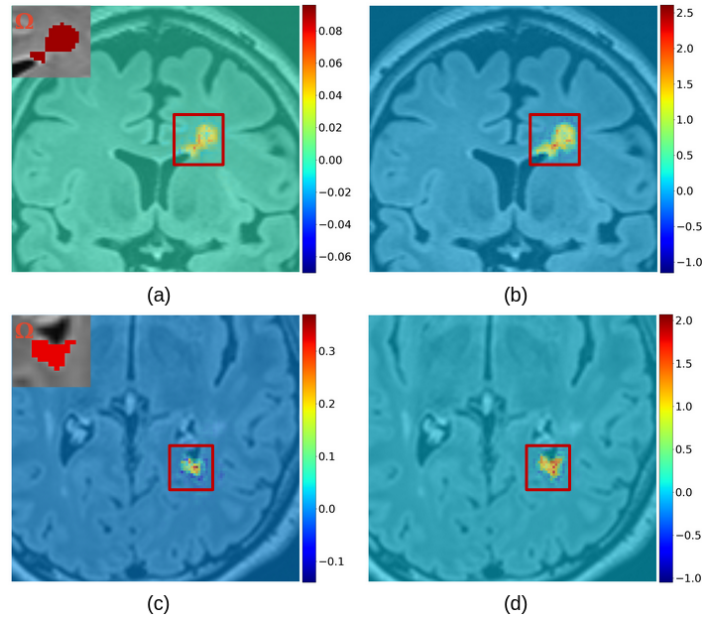


Fig. 7. Saliency maps based on SG generated for an extensive lesion, following the average (a) and the maximum (b) methodology. Saliency maps generated for a smaller lesion, following the average (c) and the maximum (d) methodology. The thumbnails illustrate the lesion domains Ω used during the computation.

3.2. Assessing the contributions of input MR sequences using gradient-based saliency maps

Saliency maps (based on SG) generated with respect to FLAIR for a true positive (TP) lesion are presented in Fig. 8. Positive gradient values appeared to accumulate inside the targeted lesion domain Ω and its edges, while negative values populated its neighborhood. Following the same procedure with respect to MPRAGE, we observed an opposite trend (Fig. 9): negative values in Ω and positive around its borders. In both cases, the values dropped to zero when looking at a distance of $\sim 44mm$ from Ω 's borders, and presented close-to-zero values for other lesions in the same brain regions as Ω . The latter was also observed in the instance-level explanation method based on Grad-CAM++ (see Fig. 10). For TP cases, we observed that positive values of gradients (median and 95% confidence interval (CI) of 0.50140 ± 0.00072) computed with respect to FLAIR were consistently greater (in absolute value) than negative values for MPRAGE (median and 95% CI of -0.19584 ± 0.00031).

3.3. Statistical distribution of gradient values for TPs, FPs, FNs and TNs

Fig. 11 reports the distribution of maximum (a) and minimum (b) gradients values — with respect to FLAIR — for TN, FN, FP and TP volumes. The median value and 95% CI for positive values in each group of volumes were, respectively: 0.465 ± 0.025 (TN), 1.202 ± 0.036 (FN), 1.630 ± 0.019 (FP), and 1.997 ± 0.016 (TP). The median value and 95% CI for negative values were, respectively: -0.245 ± 0.008 (TN), -0.359 ± 0.010 (FN), -0.522 ± 0.008 (FP), and -0.639 ± 0.009 (TP). The p -value of Mann Whitney U tests run on all pairs of groups was lower than 6×10^{-65} .

3.4. Sanity checks

When inserting a synthetic lesion in a healthy region of the WM, we obtained scores higher than 0.3, enough to trigger its segmentation. In this case, the saliency map (based on SG) resembled those obtained for true WM lesions. However, when the same lesion was placed outside the skull, the lesion domain presented scores below the threshold after the Softmax activation and, thus, the lesion was not detected. In the saliency map, we observed a few positive peak values, but the rest of the lesion volume had negative or close-to-zero gradients. Similarly to the second case, when the lesion and part of its surrounding tissue were moved outside the skull, we noticed low prediction scores. The saliency map, however, presented higher peak values than the second experiment. The prediction scores after the Softmax and the saliency maps for all these three cases were reported in Fig. 12.

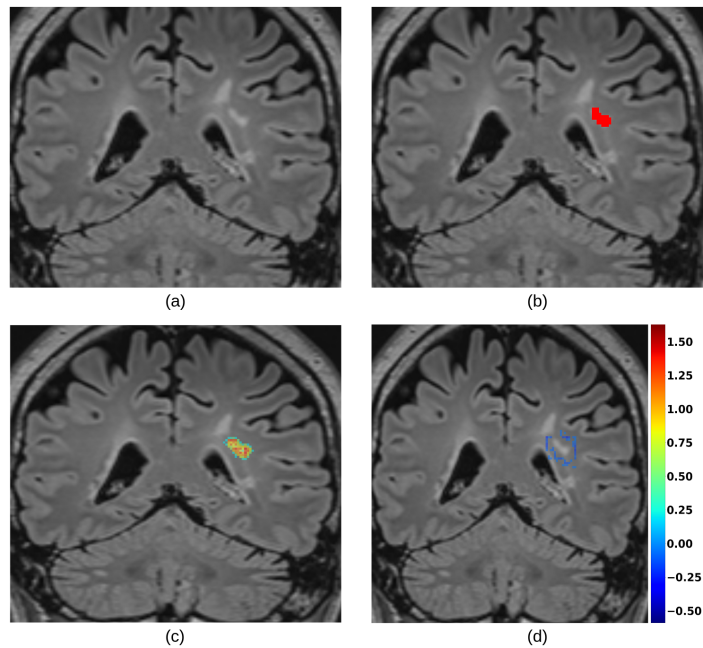


Fig. 8. Example of a FLAIR image (a), the lesion domain Ω (b), and the corresponding saliency map obtained with the proposed adaptation of SmoothGrad isolating positive (c) and negative (d) gradients. Values in $[-0.05, 0.2]$ are not displayed to focus on most significant saliency.

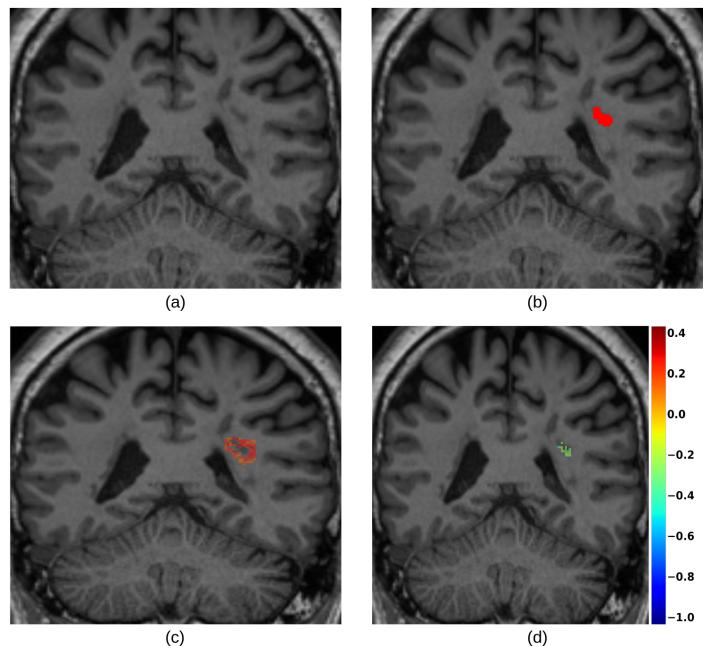


Fig. 9. Example of an MPRAGE image (a), the lesion domain Ω (b), and the corresponding saliency map obtained with the proposed adaptation of SmoothGrad isolating positive (c) and negative (d) gradients. Values in $[-0.1, 0.1]$ are not displayed to focus on the most significant saliency.

3.5. Experiment on contextual information

The experiment on contextual information showed that, compared to a lesion without any surroundings (i.e., constant background values outside the lesion mask), the prediction score for a lesion increased when including voxels belonging to its perilesional healthy tissue. The prediction score reached a plateau when adding tissue distant 12 – 15mm from the lesion border. A minimum of 7mm of healthy perilesional tissue allowed to correctly segment all the 178 WM lesions, as reported in Fig. 13. The standard deviation reached a peak at 3mm distance from lesion’s border, meaning that some lesions already presented high scores while others had not yet been segmented.

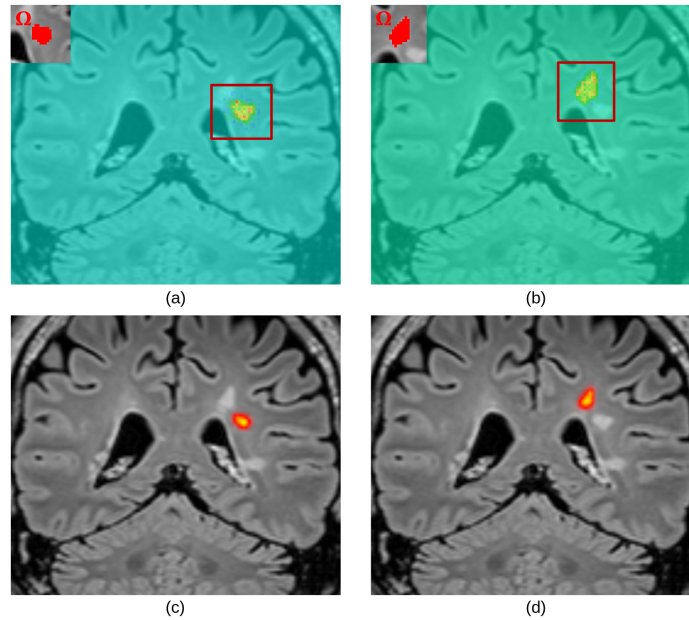


Fig. 10. Saliency maps obtained with the proposed adaptation of SmoothGrad for two close lesions (a) and (b). Heatmaps obtained with the proposed adaptation of Grad-CAM++ for the same two lesions (c) and (d). The thumbnails illustrate the lesion domains Ω used during the computation.

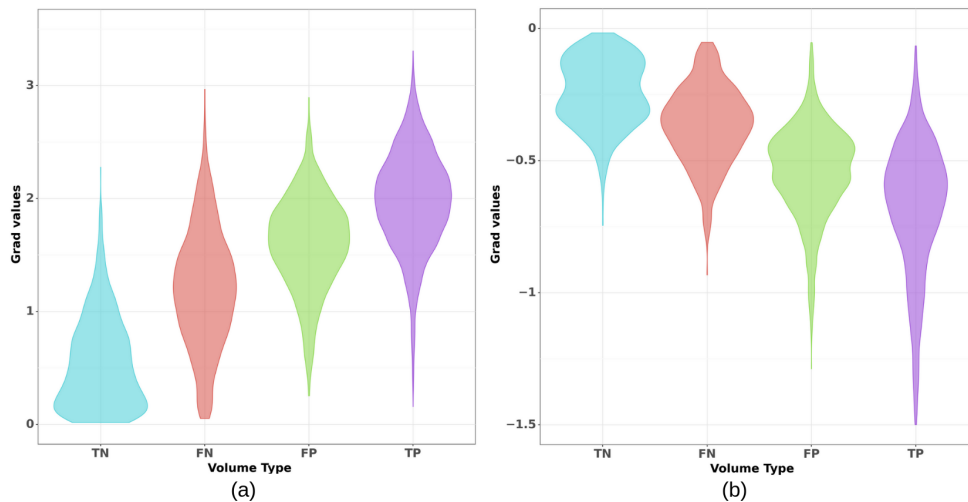


Fig. 11. Violin plots representing the distribution of saliency maps maximum (a) and minimum (b) values. The four distributions refer to TN, FN, FP and TP volumes.

4. Discussion

Our study demonstrated the successful adaptation of two existing XAI methods to the task of semantic segmentation. Specifically, we are able to generate quantitative explanation maps for single segmented instances, such as MS lesions.

The distribution of values in the saliency maps generated with SG showed that FLAIR imaging had a more significant contribution to the segmentation of lesions, compared to MPRAGE. This resonates with the fact that FLAIR offers a better contrast for common MS lesions in the WM, such as periventricular and sub-cortical, since the signal from the cerebrospinal fluid is suppressed. Only a part of these lesions are clearly visible in T1-weighted images, such as MPRAGE, which are preferred to detect cortical plaques (Trip and Miller, 2005; Nelson *et al.*, 2008).

For a lesion domain Ω , saliency maps (based on SG) with respect to FLAIR presented positive and negative gradients, respectively distributed inside Ω and in its neighborhood (Figs. 8 and 9). Indeed, positive gradients indicate that an increase in their intensities in the MRI would suggest the presence of a lesion in Ω . Conversely, voxels with negative saliency values indicate that the presence of a lesion in Ω would be suggested by a decrease in their intensities in the MRI. The antithetic distribution of saliency values in MPRAGE is due to the fact that WM lesions appear as hyperintense in FLAIR and as hypointense in MPRAGE, compared to the healthy WM.

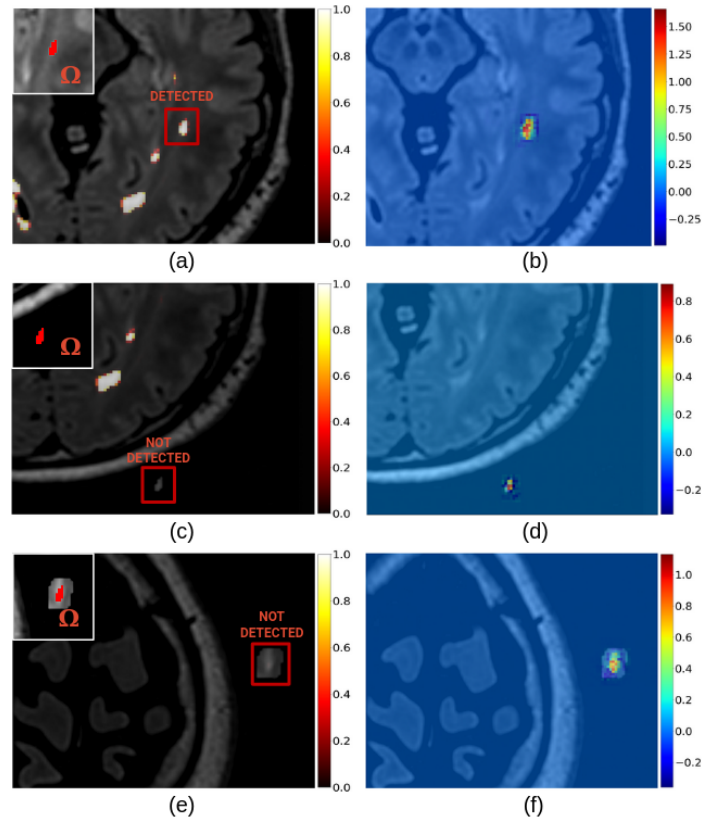


Fig. 12. The prediction score before the Softmax for the case of a lesion artificially placed in the WM (a), in the background without (c) and with (e) a part of the surrounding WM. The corresponding saliency maps (b), (d) and (f), respectively. Only the synthetic lesion in the WM triggered a detection.

Both of our XAI methods showed that voxels far from a lesion domain Ω did not appear to impact the prediction of voxels belonging to Ω (Fig. 10). Since we employed a CNN, each network unit did not depend on the entire input, but on a region called receptive field. Luo et al. (2016) described that the effective area of a receptive field (effective receptive field, or ERF) starts as small, and then grows during training. Furthermore, the same study described skip-connections, part of a U-Net, as a cause of the reduction of receptive field's size. In our particular case, one of the possible interpretations could be that useful features to segment a lesion were close to the lesion itself and its neighborhood, so the learned receptive field is small. For instance, it is likely that re-training our model by including the images of the contextual experiment (e.g., until dilation step 25) and labeling them as background, would lead the model to have a larger ERF. Saliency maps, after such re-training, may show a higher attention to neighbouring tissue at a greater distance from a lesion border.

Peak values of saliency maps generated for the four groups of volumes (TP, FP, FN and TN) presented distributions that are significantly different from each other (Fig. 11). This suggests that, even if not segmented, FN volumes captured the model's attention notably more than TN volumes during inference. A similar conclusion can be drawn for TP and FP volumes. In both cases, our quantitative saliency maps could help increase the sensitivity and specificity of the model. However, in the case of FN volumes, some external input would be needed to select the lesion domain for computation. Such input could be that of a neurologist (for brain lesions), or could be derived from other maps, perhaps based on prediction's uncertainty.

Experiments on synthetic lesions suggested that the location of a lesion in the WM was not as important as the intensity of voxels within the lesion and its neighborhood (Fig. 12). The described behavior is expected, since we used a patch-based network. This, along with FLAIR's importance over MPRAGE, would support the hypothesis that the model's predictions rely predominantly on voxel intensities inside lesions in FLAIR.

However, the last experiment on contextual information revealed that high and stable prediction scores were related to the amount of contextual healthy brain tissue from the perilesional volume (Fig. 13). Enriching the context around the lesion in the input resulted in an increase of prediction scores up to a distance of 12 – 15mm from the lesion border. Past this distance, additional voxels no longer impact the prediction as seen by the plateau in Fig. 13(B). A possible conclusion is that a patch size of $96mm^3$ could have been unnecessarily large for most lesions. Furthermore, it would be interesting to test if the patch size during training would have a potential influence on the plateau's position of Fig. 13(B). We might expect that bigger patches would make the model require more contextual information to segment a lesion.

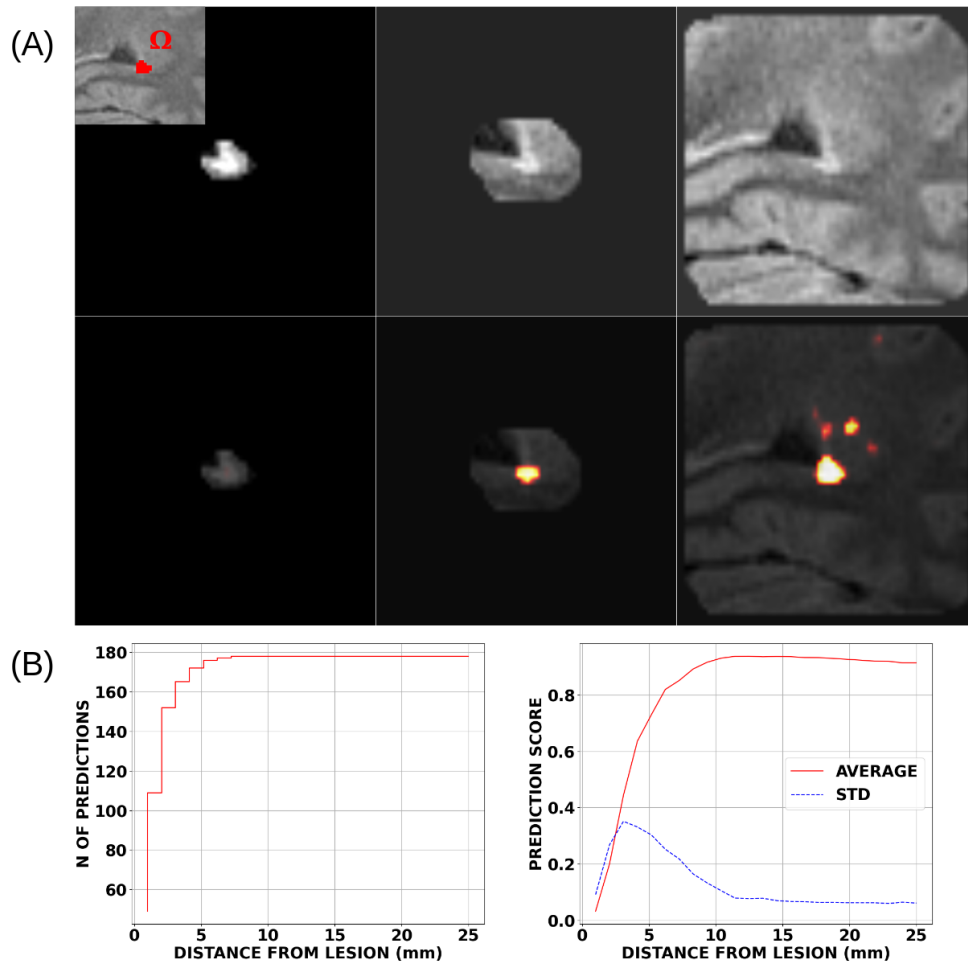


Fig. 13. (A): FLAIR masked out with dilation steps 1, 5 and 24 (top), and the corresponding output probability maps (bottom). (B): Plots representing the number of segmented lesions (top) and the average and standard deviation across patients of the mean prediction score (bottom) at each dilation step.

5. Conclusion

We adapted two XAI methods to provide quantitative instance-level explanations for segmentation, which we applied to the specific case of MS lesion segmentation. The analysis of the explanation maps and additional tests revealed fundamental insights into the decision mechanism of a deep neural network, which could also be used to orient architecture choices (e.g., patch size), and to boost the sensitivity/specificity of the model. The acquired new knowledge can be an important step in facilitating AI integration into clinical practice. The proposed methods can potentially be applied to various segmentation tasks outside the medical imaging field, such as autonomous driving and robotics.

Acknowledgments

This work was supported by the Hasler Foundation with the project MSxplain number 21042, the Swiss National Science Foundation (SNSF) with the project 205320_219430, and the Swiss Cancer Research foundation with the project TARGET (KFS-5549-02-2022-R). We acknowledge access to the expertise of the CIBM Center for Biomedical Imaging, a Swiss research center of excellence founded and supported by CHUV, UNIL, EPFL, UNIGE and HUG.

References

- Agarwal, S., Jabbari, S., Agarwal, C., Upadhyay, S., Zhiwei, S.W., Lakkaraju, H., 2021. Towards the unification and robustness of perturbation and gradient based explanations, in: Proceedings of the 38th International Conference on Machine Learning, pp. 110–119. doi:10.48550/arXiv.2102.10618.
- Alrabai, A., Echtioui, A., Hamida, A., 2022. Multiple Sclerosis Segmentation using Deep Learning Models : Comparative Study, in: 2022 6th International Conference on Advanced Technologies for Signal and Image Processing (ATSIP), pp. 1–6. doi:10.1109/ATSIP5956.2022.9805983.
- Arun, N., Gaw, N., Singh, P., Chang, K., Aggarwal, M., Chen, B., Hoebel, K., Gupta, S., Patel, J., Gidwani, M., Li, M., Kalpathy-Cramer, J., 2021. Assessing the (Un)Trustworthiness of Saliency Maps for Localizing Abnormalities in Medical Imaging. Radiology: Artificial Intelligence 3. doi:10.1148/ryai.2021200267.

- Baselli, G., Codari, M., Sardanelli, F., 2020. Opening the black box of machine learning in radiology: can the proximity of annotated cases be a way? *European Radiology Experimental* 4. doi:10.1186/s41747-020-00159-0.
- Chattopadhyay, A., Sarkar, A., Howlader, P., Balasubramanian, V.N., 2018. Grad-CAM++: Generalized Gradient-Based Visual Explanations for Deep Convolutional Networks, in: 2018 IEEE Winter Conference on Applications of Computer Vision (WACV), pp. 839–847. doi:10.1109/WACV.2018.00097.
- Commowick, O., Combès, B., Cervenansky, F., Dojat, M., 2023. Editorial: Automatic methods for multiple sclerosis new lesions detection and segmentation. *Frontiers in Neuroscience* 17. doi:10.3389/fnins.2023.1176625.
- Cordts, M., Omran, M., Ramos, S., Rehfeld, T., Enzweiler, M., Benenson, R., Franke, U., Roth, S., Schiele, B., 2016. The Cityscapes Dataset for Semantic Urban Scene Understanding, in: 2016 IEEE Conference on Computer Vision and Pattern Recognition (CVPR), pp. 3213–3223. doi:10.1109/CVPR.2016.350.
- Depeursinge, A., Andrearczyk, V., Whybra, P., van Griethuysen, J., Müller, H., Schaefer, R., Vallières, M., Zwanenburg, A., 2020. Standardised convolutional filtering for radiomics. *arXiv* doi:10.48550/arXiv.2006.05470.
- Díaz-Hurtado, M., Martínez-Heras, E., Solana, E., Casas-Roma, J., Llufríu, S., Kanber, B., Prados, F., 2022. Recent advances in the longitudinal segmentation of multiple sclerosis lesions on magnetic resonance imaging: a review. *Neuroradiology* 64. doi:10.1007/s00234-022-03019-3.
- Goh, G.S.W., Lapuschkin, S., Weber, L., Samek, W., Binder, A., 2021. Understanding Integrated Gradients with SmoothTaylor for Deep Neural Network Attribution, in: 2020 25th International Conference on Pattern Recognition (ICPR), pp. 4949–4956. doi:10.1109/ICPR48806.2021.9413242.
- Hemond C, C., Bakshi, R., 2018. Magnetic Resonance Imaging in Multiple Sclerosis. *old Spring Harbor perspectives in medicine* 8, 5. doi:10.1101/cshperspect.a028969.
- Jonkman, L., Soriano, A., Amor, S., Barkhof, F., Valk, P., Vrenken, H., Geurts, J., 2015. Can ms lesion stages be distinguished with mri? a postmortem mri and histopathology study. *Journal of neurology* 262. doi:10.1007/s00415-015-7689-4.
- Klein, S., Staring, M., Murphy, K., Viergever, M., Pluim, J., 2009. Elastix: A Toolbox for Intensity-Based Medical Image Registration. *IEEE transactions on medical imaging* 29, 196–205. doi:10.1109/TMI.2009.2035616.
- Kobayashi, K., Alam, S.B., 2024. Explainable, interpretable, and trustworthy ai for an intelligent digital twin: A case study on remaining useful life. *Engineering Applications of Artificial Intelligence* 129, 107620. doi:10.1016/j.engappai.2023.107620.
- Kofler, F., Shit, S., Ezhov, I., Fidon, L., Horvath, I., Al-Maskari, R., Li, H., Bhatia, H., Loehr, T., Piraud, M., Erturk, A., Kirschke, J., Peeken, J., Vercauteren, T., Zimmer, C., Wiestler, B., Menze, B., 2022. Blob loss: instance imbalance aware loss functions for semantic segmentation. *arXiv* doi:10.48550/ARXIV.2205.08209.
- Koftuniuk, A., Pawlak, B., Krówczyńska, D., Chojdak-Lukasiewicz, J., 2023. The quality of life in patients with multiple sclerosis – Association with depressive symptoms and physical disability: A prospective and observational study. *Frontiers in Psychology* 13, 1068421. doi:10.3389/fpsyg.2022.1068421.
- Luo, W., Li, Y., Urtasun, R., Zemel, R., 2016. Understanding the effective receptive field in deep convolutional neural networks, in: 30th Conference on Neural Information Processing Systems (NIPS 2016), pp. 839–847. doi:10.1109/WACV.2018.00097.
- Ma, Y., Zhang, C., Cabezas, M., Song, Y., Tang, Z., Liu, D., Cai, W., Barnett, M., Wang, C., 2022. Multiple Sclerosis Lesion Analysis in Brain Magnetic Resonance Images: Techniques and Clinical Applications. *IEEE Journal of Biomedical and Health Informatics* PP, 1–1. doi:10.1109/JBHI.2022.3151741.
- Mahapatra, D., Poellinger, A., Reyes, M., 2022. Interpretability-Guided Inductive Bias For Deep Learning Based Medical Image. *Medical Image Analysis* 81, 102551. doi:10.1016/j.media.2022.102551.
- Maier-Hein, L., Reinke, A., Christodoulou, E., Glocker, B., Godau, P., Isensee, F., Kleesiek, J., Kozubek, M., Reyes, M., Riegler, M., Wiesenfarth, M., Baumgartner, M., Eisenmann, M., Heckmann-Nötzel, D., Kavr, A., Radsch, T., Tizabi, M.D., Acion, L., Antonelli, M., Jaeger, P., 2022. Metrics reloaded: Pitfalls and recommendations for image analysis validation. *arXiv.org* doi:10.48550/arXiv.2206.01653.
- McKnight, P.E., Najab, J., 2010. Mann-Whitney U Test. *John Wiley & Sons, Ltd.* doi:10.1002/9780470479216.corpsy0524.
- Nelson, F., Poonawalla, A., Hou, P., Wolinsky, J., Narayana, P., 2008. 3d mprage improves classification of cortical lesions in multiple sclerosis. *Multiple sclerosis (Houndmills, Basingstoke, England)* 14, 1214–9. doi:10.1177/1352458508094644.
- Raina, V., Molchanova, N., Graziani, M., Malinin, A., Muller, H., Cuadra, M.B., Gales, M., 2023. Tackling Bias in the Dice Similarity Coefficient: Introducing NDSC for White Matter Lesion Segmentation, in: 2023 IEEE 20th International Symposium on Biomedical Imaging (ISBI), pp. 1–5. doi:10.1109/ISBI53787.2023.10230755.
- Rajpurkar, P., Irvin, J., Zhu, K., Yang, B., Mehta, H., Duan, T., Ding, D., Bagul, A., Langlotz, C., Shpanskaya, K., Lungren, M., Ng, A., 2017. CheXNet: Radiologist-Level Pneumonia Detection on Chest X-Rays with Deep Learning. *arXiv* doi:10.48550/arXiv.1711.05225.
- Saranya, A., Subhashini, R., 2023. A systematic review of Explainable Artificial Intelligence models and applications: Recent developments and future trends. *Decision Analytics Journal* 7, 100230. doi:10.1016/j.dajour.2023.100230.
- Selvaraju, R.R., Cogswell, M., Das, A., Vedantam, R., Parikh, D., Batra, D., 2017. Grad-cam: Visual explanations from deep networks via gradient-based localization, in: 2017 IEEE International Conference on Computer Vision (ICCV), pp. 618–626. doi:10.1109/ICCV.2017.74.
- Shamonin, D., Bron, E., Lelieveldt, B., Smits, M., Klein, S., Staring, M., 2014. Fast Parallel Image Registration on CPU and GPU for Diagnostic Classification of Alzheimer's Disease. *Frontiers in neuroinformatics* 7, 50. doi:10.3389/fninf.2013.00050.
- Simonyan, K., Vedaldi, A., Zisserman, A., 2013. Deep Inside Convolutional Networks: Visualising Image Classification Models and Saliency Maps. 2nd International Conference on Learning Representations, ICLR 2014, Banff, AB, Canada, April 14–16, 2014, Workshop Track Proceedings.
- Singh, R.K., Gorantla, R., Allada, S., Narra, P., 2022. SkiNet: A deep learning framework for skin lesion diagnosis with uncertainty estimation and explainability. *PloS one* 17, e0276836. doi:10.1371/journal.pone.0276836.
- Smilkov, D., Thorat, N., Kim, B., Viégas, F., Wattenberg, M., 2017. SmoothGrad: removing noise by adding noise. *CoRR*.
- Spagnolo, F., Depeursinge, A., Schädelin, S., Akbulut, A., Müller, H., Baraković, M., Melie-Garcia, L., Bach Cuadra, M., Granziera, C., 2023. How far ms lesion detection and segmentation are integrated into the clinical workflow? a systematic review. *NeuroImage Clinical* 39, 103491. doi:10.1016/j.nicl.2023.103491.
- Thompson, A., Banwell, B., Barkhof, F., Carroll, W., Coetzee, T., Comi, G., Correale, J., Fazekas, F., Filippi, M., Freedman, M., Fujihara, K., Galetta, S., Hartung, H.P., Kappos, L., Lublin, F., Marrie, R., Miller, A., Miller, D., Montalban, X., Cohen, J., 2017. Diagnosis of multiple sclerosis: 2017 revisions of the McDonald criteria. *The Lancet Neurology* 17. doi:10.1016/S1474-4422(17)30470-2.
- Trip, S.A., Miller, D.H., 2005. Imaging in multiple sclerosis. *Journal of Neurology, Neurosurgery & Psychiatry* 76, 11–18. doi:10.1136/jnnp.2005.073213.
- Tustison, N., Avants, B., Cook, P., Zheng, Y., Egan, A., Yushkevich, P., Gee, J., 2010. N4itk: improved n3 bias correction. *Medical Imaging, IEEE Transactions on* 29, 1310–1320. doi:10.1109/TMI.2010.2046908.
- Varatharasan, V., Shin, H.S., Tsourdos, A., Colosimo, N., 2019. Improving Learning Effectiveness For Object Detection and Classification in Cluttered Backgrounds, in: 2019 Workshop on Research, Education and Development of Unmanned Aerial Systems (RED UAS), pp. 78–85. doi:10.1109/REDUAS47371.2019.899695.
- Vinogradova, K., Dibrov, A., Myers, G., 2020. Towards Interpretable Semantic Segmentation via Gradient-weighted Class Activation Mapping, in: Thirty-Fourth AAAI Conference on Artificial Intelligence (AAAI 2020), pp. 13943–13944. doi:10.1609/aaai.v34i10.7244.
- de Vries, B., Zwezerijnen, G., Burchell, G., van Velden, F., Menke-van der Houven van Oordt, C., Boellaard, R., 2023. Explainable artificial intelligence (XAI) in radiology and nuclear medicine: a literature review. *Frontiers in Medicine* 10. doi:10.3389/fmed.2023.1180773.
- Wickstrøm, K., Kampffmeyer, M., Jenssen, R., 2020. Uncertainty and interpretability in convolutional neural networks for semantic segmentation of colorectal

- polyps. *Medical Image Analysis* 60, 101619. doi:10.1016/j.media.2019.101619.
- Yang, J., Hamade, M., Wu, Q., Wang, Q., Axtell, R., Giri, S., Mao-Draayer, Y., 2022. Current and Future Biomarkers in Multiple Sclerosis. *International journal of molecular sciences* 23. doi:10.3390/ijms23115877.
- Zeng, C., Gu, L., Liu, Z., Zhao, S., 2020. Review of Deep Learning Approaches for the Segmentation of Multiple Sclerosis Lesions on Brain MRI. *Frontiers in Neuroinformatics* 14. doi:10.3389/fninf.2020.610967.
- Çiçek, O., Abdulkadir, A., Lienkamp, S.S., Brox, T., Ronneberger, O., 2016. 3D U-Net: Learning Dense Volumetric Segmentation from Sparse Annotation. *arXiv* doi:10.48550/ARXIV.1606.06650.